J. Fluid Mech. (2012), *vol.* 694, *pp.* 78–99. © Cambridge University Press 2012
doi:10.1017/jfm.2011.504

Sedimentation of a sphere in a viscoelastic fluid: a multiscale simulation approach

A. Abedijaberi and B. Khomami†

Material Research & Innovation Laboratory (MRAIL), Department of Chemical & Biomolecular Engineering, University of Tennessee in Knoxville, Knoxville, TN 37996-5334, USA

(Received 24 July 2011; revised 4 October 2011; accepted 11 November 2011; first published online 18 January 2012)

A long-standing problem in non-Newtonian fluid mechanics, namely the relationship between drag experienced by a sphere settling in a tube filled with a dilute polymeric solution and the sphere sedimentation velocity, is investigated via self-consistent multiscale flow simulations. Comparison with experimental measurements by Arigo *et al.* (*J. Non-Newtonian Fluid Mech.*, vol. 60, 1995, pp. 225–257) have revealed that the evolution of the drag coefficient as a function of fluid elasticity can be accurately predicted when the macromolecular dynamics is described by realistic micromechanical models that closely capture the transient extensional viscosity of the experimental fluid at high extension rates. Specifically, for the first time we have computed the drag coefficient on the sphere at high Weissenberg number *Wi* utilizing multi-segment bead–spring chain models with appropriate molecular parameters and have demonstrated that a hi-fidelity multiscale simulation is not only capable of accurately describing the drag on the sphere as a function of *Wi* at various sphere-to-tube diameter ratios but also it can closely reproduce the experimentally observed velocity and stresses in the wake of the sphere.

Key words: computational methods, viscoelasticity

1. Introduction

One of the principal concerns of fluid mechanics is to develop a fundamental and quantitative understanding of global variables such as pressure drop, hydrodynamic drag and dissipation as functions of flow rate, geometry and boundary conditions. The technological importance of such knowledge cannot be overemphasized. For Newtonian flows, especially under laminar flow conditions, these relationships can be easily determined using either well-established analytical techniques or with the aid of readily available commercial software packages. However for polymeric flows, despite the tremendous progress in development of numerical techniques and constitutive theories in the past decade, continuum-level computations are still incapable of quantitatively predicting macroscopic variables such as frictional resistance enhancement (FRE) in prototypical extension-dominated, mixed kinematics creeping flows of dilute polymeric solutions such as contraction/expansion flows (Quinzani, Armstrong & Brown 1994; Rothstein & McKinley 1999, 2001; Koppol *et al.* 2009),

† Email address for correspondence: bkhomami@utk.edu

https://doi.org/10.1017/jfm.2011.504 Published online by Cambridge University Press

and flow past bluff objects (Baaijens *et al.* 1994, 1995; Arigo *et al.* 1995; Li *et al.* 1998, 2000; Yang & Khomami 1999).

In the past two decades, coordinated experimental/computational studies of dilute polymeric solutions in a number of benchmark problems have clearly demonstrated that the aforementioned lack of quantitative prediction of FRE is due to the inability of constitutive equations to quantitatively capture the polymeric body forces that result from the configurational complexity of the macromolecules in mixed kinematics flows with strong straining components (Lunsmann *et al.* 1993; Satrape & Crochet 1994; Arigo *et al.* 1995; Talwar & Khomami 1995; Rasmussen & Hassager 1996; Perkins, Smith & Chu 1997; Li *et al.* 1998, 2000; Burghardt *et al.* 1999; Yang & Khomami 1999; Grillet, Yang & Khomami 1999; McKinley 2001; Abedijaberi *et al.* 2008; Abedijaberi & Khomami 2011). In fact this realization has been the main motivating factor for the development of multiscale simulation techniques that couple kinetic theory based micromechanical models for polymer dynamics at the mesoscopic level with macroscopic equations of mass and momentum conservation to self-consistently capture the intricate coupling between flow deformation and macromolecular configuration during flow (Laso & Öttinger 1993; Öttinger, van den Brule & Hulsen 1997; Hulsen, van Heel & van den Brule 1997; Halin *et al.* 1998; Somasi & Khomami 2000, 2001; Wapperom, Keunings & Legat 2000; Gigras & Khomami 2002). However, despite significant algorithmic advances in the past several years, multiscale flow simulation techniques still remain highly computationally intensive in comparison to their continuum-level counterparts. Hence, to date most of the large-scale complex kinematics multiscale flow simulations of dilute polymeric solutions have been performed with the simplest micromechanical model for polymer molecules, namely the elastic dumbbell model. Although this class of simulations has provided significant insight in understanding the influence of closure approximations on prediction of polymeric stresses in mixed kinematics flows of dilute polymeric solutions, they are still unable to quantitatively predict FRE and other important flow quantities such as vortex dynamics, velocity and stress wake structure in creeping-flow benchmark problems such as contraction/expansions flows or flow past bluff objects (Verhoef, van den Brule & Hulsen 1999; Rothstein & McKinley 1999, 2001; Wapperom *et al.* 2000).

The inability of multiscale simulations with single-segment kinetic-theory-based models to provide quantitative prediction of macroscopic flow quantities in extension-dominated complex kinematics flows can be rationalized in terms of recent fluorescence microscopy studies of model macromolecules, namely DNA, under flow that have demonstrated the necessity of multi-segment micromechanical models such as bead–rod and bead–spring chains for quantitative prediction of macromolecular dynamics (Doyle, Shaqfeh & Spiegelberg 1998; Somasi & Khomami 2000, 2001; Shaqfeh 2005; Larson 2005; Thomas, DePuit & Khomami 2009). These findings clearly underscore the fact that a multi-segment description of the macromolecule or reduced-order coarse-grained models capable of retaining the essential physics associated with the internal degrees of freedom of the macromolecule are required for accurate modelling of dilute polymer solutions under flow (Venkataramani, Sureshkumar & Khomami 2008*a*,*b*). To this end, we have recently performed multiscale simulations of flow of a highly elastic dilute polymeric solution through a 4:1:4 axisymmetric contraction and expansion geometry and for the first time demonstrated that the pressure drop evolution as a function of flow rate can be accurately predicted when the chain dynamics is described by multi-segment bead–spring micromechanical models that closely capture the transient extensional

https://doi.org/10.1017/jfm.2011.504 Published online by Cambridge University Press

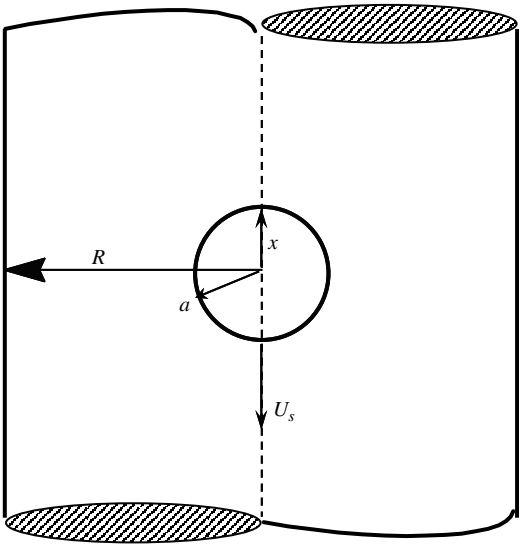


FIGURE 1. Schematic of the sedimentation of a sphere in a tube; $\chi = a/R$.

viscosity of the experimental fluid. Specifically, for the first time the experimentally observed doubling of the dimensionless excess pressure drop at intermediate flow rates was predicted (Koppol *et al.* 2009).

Motivated by the aforementioned success in quantitatively describing the FRE in flow of dilute polymeric solutions in contraction/expansion flows, we have turned our attention to flow of dilute polymeric solutions past bluff objects. This choice has been motivated by the fact that in creeping viscoelastic flows past objects such as cylinders or spheres the relationship between FRE and the flow rate and the wake structure (velocity and stresses) cannot be accurately predicted by continuum-level or multiscale simulations with simple micromechanical models (Lunsmann *et al.* 1993; Baaijens *et al.* 1994, 1995; Satrape & Crochet 1994; Arigo *et al.* 1995; Rasmussen & Hassager 1996; Yang & Khomami 1999; McKinley 2001; Somasi 2001). Specifically, in the case of the two well-known benchmark flow problems, namely flow past a cylinder in a channel and sedimentation of a sphere in a tube, utilization of commonly used constitutive equations such as the FENE-P and the Giesekus models for significantly strain-hardening fluids leads to unrealistically large localized polymeric stresses and stress gradients in the wake of the object, thereby preventing accurate prediction of FRE and the wake structure (Baaijens *et al.* 1994, 1995; Somasi 2001; Abedijaberi & Khomami 2011). To this end, results of a self-consistent multiscale flow simulation of sedimentation of a sphere in a tube filled with a Boger fluid composed of 0.21 wt% polyisobutylene (PIB), 4.83 wt% tetradecane (C14), and 94.86 wt% polybutene (PB), are presented that for the first time provide an accurate prediction of the enhanced drag coefficient and the extended wake structure observed experimentally at high *Wi*.

2. Problem formulation

We consider sedimentation of a sphere along the centreline of a tube filled with a dilute polymeric solution as depicted in figure 1. Specifically, we consider two geometries with sphere-to-tube radius ratios of $\chi = a/R = 0.121$ and $\chi = 0.243$. This choice has been motivated by the fact that there is a wealth of experimental data

https://doi.org/10.1017/jfm.2011.504 Published online by Cambridge University Press

on the drag coefficient and the flow kinematics of well-characterized dilute polymeric solution in these two geometries (Arigo *et al.* 1995).

2.1. *Governing equations*

The equations of motion and continuity for creeping flow of an incompressible fluid are

$$-\nabla P^* + \nabla \cdot \boldsymbol{\tau} = 0, \tag{2.1}$$

$$\nabla \cdot \boldsymbol{u} = 0, \tag{2.2}$$

where $P^* = P + \rho g h$, and P, $\boldsymbol{u}$, ρ, g, h and $\boldsymbol{\tau}$ are the isotropic pressure, velocity vector, fluid density, gravitational acceleration, fluid height and deviatoric stress tensor, respectively. The governing equations are non-dimensionalized with respect to the sphere radius a, and the terminal velocity of the sphere, U_s. Hence, U_s/a is the characteristic shear rate. The pressure, P^* and the stress tensor, $\boldsymbol{\tau}$, have been made dimensionless with respect to $\eta_0 U_s/a$ in which η_0 is the fluid zero shear viscosity.

The system of equations is closed by selecting an appropriate constitutive equation or a micromechanical model for the deviatoric stress. In this study we have chosen to split the deviatoric stress into a polymeric and a solvent contribution:

$$\boldsymbol{\tau} = \boldsymbol{\tau}_s + \boldsymbol{\tau}_p \tag{2.3}$$

where the solvent contribution to the deviatoric stress is assumed to be Newtonian

$$\boldsymbol{\tau}_s = 2\beta\dot{\boldsymbol{\gamma}}. \tag{2.4}$$

In the above equation, $\beta = \eta_s/\eta_0$ is the ratio of the solvent to the total viscosity and $\dot{\boldsymbol{\gamma}}$ is the rate-of-deformation tensor, which is defined as

$$\dot{\boldsymbol{\gamma}} = \tfrac{1}{2}(\nabla \boldsymbol{u} + (\nabla \boldsymbol{u})^t). \tag{2.5}$$

We have used closed-form constitutive equations and a kinetic-theory-based elastic dumbbell or a bead–spring chain model to evaluate the polymer's contribution, $\boldsymbol{\tau}_p$, to the deviatoric stress. When the polymer dynamics is described by a FENE (finitely extensible nonlinear elastic) bead–spring chain or a FENE dumbbell (two beads connected via an entropic spring), $\boldsymbol{\tau}_p$ is evaluated using Kramers' expression (Bird *et al.* 1987):

$$\boldsymbol{\tau}_p = \left(\frac{1-\beta}{Wi}\right)\left(\frac{b_s+5}{b_s}\right)\sum_{i=1}^{N}(\langle \boldsymbol{F}_i \boldsymbol{Q}_i\rangle - \langle \boldsymbol{F}_i \boldsymbol{Q}_i\rangle_{eqlb}) \tag{2.6}$$

where Wi defined as $Wi = \lambda U/a$, λ is the relaxation time of polymer molecules, N is the number of segments in the bead–spring chain, $b_s = NHQ_0^2/k_BT$, Q_0 is the maximum extensibility of each segment, H is the spring constant, $\boldsymbol{Q}_i$ is the segmental connectivity vector which is non-dimensionalized with respect to its equilibrium length $\sqrt{k_bT/H}$, $\langle \boldsymbol{F}_i \boldsymbol{Q}_i\rangle_{eqlb} = \boldsymbol{\delta}$, $\boldsymbol{\delta}$ is the unit tensor and $\langle\cdot\rangle$ is the average (or the expectation) over the entire ensemble ($O(10^3)$ macromolecules), and $\boldsymbol{F}_i$ is the nonlinear FENE force law for the ith segment given by

$$\boldsymbol{F}_i = \frac{\boldsymbol{Q}_i}{1-(NQ_i^2/b_s)}. \tag{2.7}$$

The temporal evolution of the segmental connectivity vector $\boldsymbol{Q}_i$ of the ith segment of the FENE bead–spring model under flow is determined using the BCF (Brownian

https://doi.org/10.1017/jfm.2011.504 Published online by Cambridge University Press

configuration field) approach (Hulsen *et al.* 1997; Somasi & Khomami 2000; Somasi *et al.* 2002; Koppol, Sureshkumar & Khomami 2007; Koppol *et al.* 2009) since it is ideally suitable for implementation in the finite-element context. The BCF evolution equation for the segmental connectivity is given as

$$\mathrm{d}\boldsymbol{Q}_i(x,t) = \left[-\boldsymbol{u}(x,t)\cdot\nabla\boldsymbol{Q}_i(x,t) + \boldsymbol{\kappa}(x,t)\cdot\boldsymbol{Q}_i(x,t) - \frac{\boldsymbol{F}_i^E}{4Wi}\right]\mathrm{d}t + \sqrt{\frac{1}{2Wi}}[\mathrm{d}\boldsymbol{W}_{i+1}(t) - \mathrm{d}\boldsymbol{W}_i(t)] \tag{2.8}$$

where

$$\boldsymbol{F}_i^E = \begin{cases} -2\boldsymbol{F}_i + \boldsymbol{F}_{i+1}, & i = 1, \\ \boldsymbol{F}_{i-1} - 2\boldsymbol{F}_i + \boldsymbol{F}_{i+1}, & 1 < i < N, \\ \boldsymbol{F}_{i-1} - 2\boldsymbol{F}_i, & i = N, \end{cases} \tag{2.9}$$

and $\boldsymbol{\kappa}$ is the transpose of the velocity gradient (i.e. $\boldsymbol{\kappa} = (\nabla\boldsymbol{u})^t$) and $\mathrm{d}\boldsymbol{W}_i(t)$ is the Wiener process which accounts for the Brownian force experienced by the ith bead. The Wiener process is mathematically represented by a Gaussian random vector with zero mean and variance $\mathrm{d}t$, the time step in the problem. We have also used a multi-mode FENE dumbbell model in this study where the total deviatoric stress is calculated as

$$\boldsymbol{\tau}_p = \sum_{i=1}^{M} \boldsymbol{\tau}_{p_i} \tag{2.10}$$

where M is the number of modes and $\boldsymbol{\tau}_{p_i}$ is obtained by solving (2.8) for each mode.

To arrive at a closed-form constitutive equation for the FENE dumbbell model, i.e. FENE-P constitutive equation, the Peterlin approximation is used (Bird *et al.* 1987),

$$\boldsymbol{F} \cong \frac{\boldsymbol{Q}}{1 - \langle Q^2\rangle/b} \tag{2.11}$$

where $\langle Q^2\rangle$ is the ensemble average of the square of the end-to-end distance and b is the maximum extensibility of the dumbbell. Utilizing this form of the force law, a closed-form constitutive equation to describe $\boldsymbol{\tau}_p$ is obtained as follows:

$$\boldsymbol{\tau}_p + Wi\,(\boldsymbol{\tau}_p/f)_{(1)} + (1-\beta)\,(\boldsymbol{\delta}/f)_{(1)} = 0 \tag{2.12}$$

$$f = \frac{b + 3 + (Wi/(1-\beta))\,\boldsymbol{Tr}(\boldsymbol{\tau}_p)}{b} \tag{2.13}$$

where $\boldsymbol{Tr}(.)$ is the tensor trace operation.

2.2. *Computational technique*

We have used the DEVSS-G (discrete elastic viscous split stress-gradient of velocity) finite-element method to solve the set of governing equations as it is an efficient and robust technique for solving steady and time-dependent viscoelastic flow problems (Talwar & Khomami 1992; Khomami, Talwar & Ganpule 1994; Talwar, Ganpule & Khomami 1994; Guenette & Fortin 1995; Szady *et al.* 1995; Li *et al.* 1998, 2000; Somasi *et al.* 2002; Koppol *et al.* 2007). The weak forms of the momentum and mass conservation equations using the Galerkin procedure are given by

$$[(\nabla\boldsymbol{v}):(\nabla\boldsymbol{u} + (\nabla\boldsymbol{u})^t - P^*\boldsymbol{\delta} + \boldsymbol{\tau}_p - (1-\beta)(\boldsymbol{G} + \boldsymbol{G}^t))] = [\boldsymbol{v}:\boldsymbol{\sigma}]_\Gamma, \tag{2.14}$$

https://doi.org/10.1017/jfm.2011.504 Published online by Cambridge University Press

$$[q; \nabla \cdot \boldsymbol{u}] = 0, \tag{2.15}$$

$$[g{:}(\boldsymbol{G} - \nabla \boldsymbol{u})] = 0. \tag{2.16}$$

In the above equations $\boldsymbol{G}$ is the discrete interpolant for the velocity gradient ($\nabla \boldsymbol{u}$). $[a{:}b]$ (or $[a; b]$) and $[a{:}b]_\Gamma$ are the standard inner products of (a, b) in the domain Ω and on the boundary Γ, respectively; $\boldsymbol{\sigma}$ is the traction vector on the boundary. Standard polynomials based on Legendre functions are used as the weighting functions (Szabó & Babuška 1987). Specifically, we have used continuous biquadratic polynomials for the velocities and continuous bilinear polynomial for stresses, pressure and the velocity gradient (Szabó & Babuška 1987; Talwar & Khomami 1992; Talwar *et al.* 1994; Khomami *et al.* 1994; Somasi & Khomami 2000).

The FENE-P closed-form constitutive equation and the segmental connectivity vector equations are discretized using the SUPG technique (Brooks & Hughes 1982):

$$[(\boldsymbol{\tau}_p + Wi\,(\boldsymbol{\tau}_p/f)_{(1)} + (1-\beta)\,(\boldsymbol{\delta}/f)_{(1)}){:}\boldsymbol{Y}] = 0, \tag{2.17}$$

$$\left[(\mathrm{d}\boldsymbol{Q}_i - \left(-\boldsymbol{u} \cdot \nabla \boldsymbol{Q}_i + \boldsymbol{\kappa} \cdot \boldsymbol{Q}_i + \frac{1}{4Wi}\boldsymbol{F}_i^E\right)\mathrm{d}t - \sqrt{\frac{1}{2Wi}}(\mathrm{d}\boldsymbol{W}_{i+1}(t) - \mathrm{d}\boldsymbol{W}_i(t))){:}\boldsymbol{Y}\right] = 0 \tag{2.18}$$

where $\boldsymbol{Y}$ is selected from the bilinear continuous polynomial space ($p = 1$).

For the FENE dumbbell or the bead–spring chain, $\boldsymbol{\tau}_p$ is evaluated using Kramers' expression via a Galerkin projection method:

$$\left[\left(\boldsymbol{\tau}_p - \frac{(1-\beta)}{Wi^*}\sum_{i=1}^{N}(\langle \boldsymbol{F}_i\boldsymbol{Q}_i\rangle - \boldsymbol{\delta})\right){:}\boldsymbol{m}\right] = 0 \tag{2.19}$$

where $\boldsymbol{m}$ is chosen from the bilinear continuous polynomial space ($p = 1$).

2.3. *Boundary conditions*

The boundary conditions are the standard no-slip boundary condition ($u_x = u_r = 0$) on the surface of the sphere and ($u_x = 1, u_r = 0$) along the wall, with symmetry conditions ($u_r = 0, \partial u_x/\partial r = 0$) along the centreline ($r = 0$). In addition, fully developed unidirectional velocity and stress profiles are enforced at the entrance and exit of the domain. The reference value for P^* is set to zero at the exit.

2.4. *Domain discretization*

To find an approximation to the exact solution, the domain Ω is divided into a number of four-sided elements, in which the basis functions are defined. Figure 2 depicts typical domain discretizations used in this study. Mesh refinement has been performed with the criterion that upon each refinement the size of the smallest element near the front and rear stagnation points of the sphere is reduced by an order of magnitude (see table 1 for details).

3. Fluid rheology

Figure 3 depicts the experimentally measured steady shear viscosity (η) and first normal stress coefficient (Ψ_1) as a function of the shear rate ($\dot{\gamma}$). The test fluid which is a Boger fluid composed of 0.21 wt% polyisobutylene (PIB), 4.83 wt% tetradecane (C14), and 94.86 wt% polybutene (PB), has a zero shear rate viscosity

https://doi.org/10.1017/jfm.2011.504 Published online by Cambridge University Press

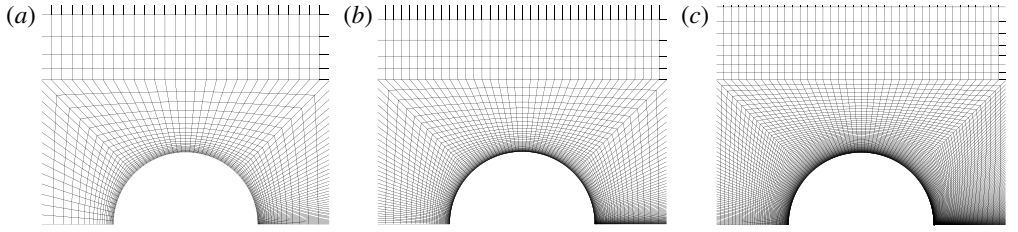


FIGURE 2. The computational domain near the surface of the sphere for meshes with 3022 elements (*a*), 7577 elements (*b*) and 18 898 elements, (*c*).

Variable	3022 elements	7577 elements	18 898 elements
DOF: $\boldsymbol{u}$	40 535	100 443	232 678
DOF: $\boldsymbol{G}$ and $\boldsymbol{\tau}$	25 288	62 344	144 128
DOF: $\boldsymbol{Q}$; $N_f = 960$	28 657 626	177 142 683	1021 399 104
Smallest element size	0.01	0.001	0.0001

TABLE 1. Degrees of freedom (DOF) for each variable and the ratio of the width of the smallest element in each mesh to that of the sphere radius.

b	η_i (Pa s)	λ_i (s)
10	3.5315	0.1
100	1.1084	1.1520
4000	1.0002	2.8395

TABLE 2. Linear viscoelastic properties of the Boger fluid composed of 0.21 wt% polyisobutylene (PIB), 4.83 wt% tetradecane (C14), and 94.86 wt% polybutene (PB). $\lambda_m = \sum_{i=1}^{2} \eta_i \lambda_i / \sum_{i=1}^{2} \eta_i = 0.7925$ s.

of $\eta_0 = 13.76$ Pa s and a solvent viscosity of $\eta_s = 8.12$ Pa s. The zero shear rate first normal stress coefficient $\Psi_{1,0} = 8.96$ Pa s^2. The ratio of the solvent viscosity to fluid zero shear viscosity defined as $\beta = \eta_s/\eta_0$ is 0.59 (Arigo *et al.* 1995).

In addition, the small-amplitude oscillatory shear flow properties of this fluid, i.e. the dynamic viscosity (η') and rigidity (η''/ω) versus the frequency of oscillation (ω), as well as its transient extensional viscosity (η^E), at various strain rates ($\dot{\epsilon}$) (Arigo *et al.* 1995) are also shown in figure 3. Various models, namely FENE bead–spring chain, FENE dumbbell, and the FENE-P closed-form constitutive equation have been used to describe the rheological behaviour of the test fluid. Linear viscoelastic fits for η' and η''/ω demonstrate that three modes are required to quantitatively describe the small-amplitude oscillatory shear flow behaviour of the solution (see table 2). The mean relaxation time of the polymer molecule (λ_m) based on these three modes is found to be 0.7925 s.

To determine the model time constant, λ_H, for the FENE dumbbell and the FENE-P constitutive equation a standard technique, namely matching of the mean relaxation time of the solution, λ_m, to the characteristic zero shear relaxation time ($\Psi_{1,0}/2\eta_{p0}$) of the model has been adopted (Somasi *et al.* 2002). In the case of the FENE

https://doi.org/10.1017/jfm.2011.504 Published online by Cambridge University Press

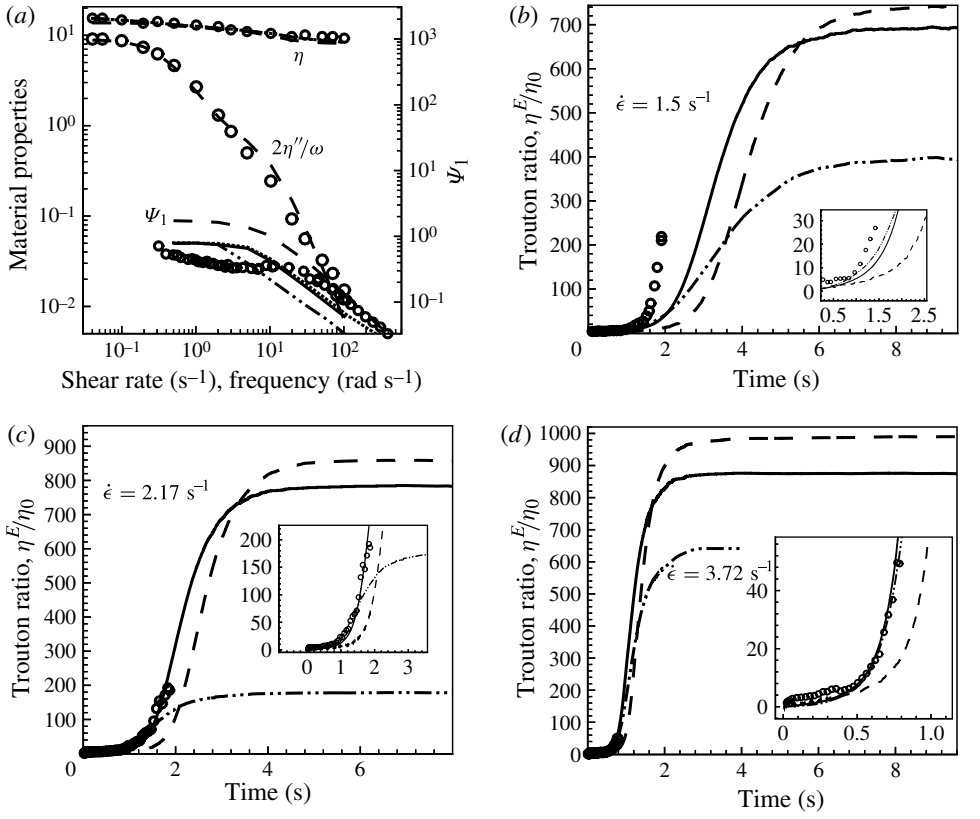


FIGURE 3. The fluid rheology of the Boger fluid composed of 0.21 wt% polyisobutylene (PIB), 4.83 wt% tetradecane (C14), and 94.86 wt% polybutene (PB) at 25 °C including: (*a*) η versus $\dot{\gamma}$, Ψ_1 versus $\dot{\gamma}$, and η''/ω versus ω; (*b*) η^E/η_0 versus ϵ at $\dot{\epsilon} = 1.53\ \mathrm{s}^{-1}$; (*c*) η^E/η_0 versus ϵ at $\dot{\epsilon} = 2.17\ \mathrm{s}^{-1}$; and (*d*) η^E/η_0 versus ϵ at $\dot{\epsilon} = 3.72\ \mathrm{s}^{-1}$. Black circles represent the experimental results, solid lines represent the 3-segment FENE bead–spring chain ($b = 4000$), dashed lines the three-mode FENE dumbbells and dash-dotted lines the FENE dumbbell ($b = 100$) respectively.

bead–spring chains, λ_H has been evaluated using the following expression (Wiest & Tanner 1989):

$$\left.\begin{aligned} \lambda_H &= \frac{\lambda_m}{d}, \\ d &= \left(\frac{b+7}{15N}\right)\left(\frac{1}{b/N+5}\right)\left(\left(2\,(N+1)^2+7\right) - \frac{12((N+1)^2+1)}{(N+1)(b/N+7)}\right). \end{aligned}\right\} \tag{3.1}$$

In the above expression, N is the number of segments in the chain and b is the maximum chain or dumbbell extensibility. For the FENE models b has been selected based on two criteria: firstly to reproduce the steady shear and the transient extensional rheology of the fluid closely and secondly to be in the range of the molecular estimates for the maximum extensibility of the PB used in the test fluid ($b \approx 5000$–$10\,000$ McKinley, Armstrong & Brown 1993). However, it should be noted that in the extension range where extensional viscosity data are available the predictions of the transient extensional rheology of the test fluid do

https://doi.org/10.1017/jfm.2011.504 Published online by Cambridge University Press

not significantly change for $4000 < b < 10\,000$, hence $b = 4000$ has been chosen to facilitate computations at high Wi where steep stress boundary layers are observed in the wake of the sphere for significant extension hardening fluids.

In the case of the multi-mode FENE model, $b = 4000$ was assigned to the mode with the longest relaxation time and other b values were chosen to optimize the fit of the transient extensional rheology of the test fluid, specifically $b = 10$ and $b = 100$. We have also performed calculations with single-mode FENE dumbbell models with $b = 10$ and $b = 100$ for comparison with the multi-mode description.

It should be noted that the rheological predictions of the FENE-based models have been obtained via Brownian dynamics simulations using a semi-implicit predictor–corrector scheme (Somasi *et al.* 2002; Koppol *et al.* 2007, 2009) with the ensemble size $N_t = 960$, while those of the FENE-P closed-form constitutive model have been obtained using the Newton–Raphson scheme described in detail in our earlier studies (Talwar & Khomami 1992; Talwar *et al.* 1994; Li *et al.* 1998, 2000; Yang & Khomami 1999).

4. Results and discussion

4.1. *Solution accuracy*

The smallest domain discretization used in this study contains 3022 elements. This level of discretization has been previously shown to provide converged solutions up to $Wi \approx 2$ at $\chi = 0.121$ and $\chi = 0.243$ in continuum-level simulation with the FENE-P constitutive equation with b in the range of 10–900 (Yang & Khomami 1999). Hence, the self-consistent multiscale simulations have been performed in three different meshes with 3022, 7577 and 18 898 elements respectively and all the reported results are based on the most refined mesh. Comparisons with different discretization levels are based on the $\tau_{p_{xx}}$ component of the polymeric stress as it exhibits large variation with Wi along the surface of the sphere and near the rear stagnation point, and it greatly influences the total drag on the sphere (Harlen, Rallison & Chilcott 1990; Baaijens *et al.* 1994, 1995; Arigo *et al.* 1995). To demonstrate the accuracy of multiscale simulations, the self-consistently computed stress profiles with the 18 898 elements mesh have been compared with those obtained based on a combined Lagrangian/Brownian dynamics (BD) technique. This approach for establishing the solution accuracy has been adopted since the conventional way of comparing solutions from multiple meshes is highly computationally intensive in the case of multiscale simulations, which is evident from the large number of degrees of freedom at each time step reported in table 1.

Similarly to our earlier studies (Koppol *et al.* 2009) the Lagrangian determination of the stress involves two steps. First, particle paths are determined via integration of the local self-consistent velocity vector ($\boldsymbol{u}$) using the fourth-order Runge–Kutta method. In turn, for the FENE model BD simulations are conducted along selected streamlines utilizing the semi-implicit predictor-scheme of Somasi *et al.* (2002) with the ensemble size $N_t = 1024$. The integrations are carried out by varying δt such that the magnitude of $\boldsymbol{u}\delta t$ is fixed to a constant. Specifically, the constant is set to A when $x \in [20, 40]$, $5A$ when $x \in [10, 20]$ and $[40, 50]$, and $25A$ when $x \in [0, 10]$ and $[50, 60]$, where x is the distance from the inlet of the tube and the centre of the sphere is at $x = 25$. With $A \approx 1 \times 10^{-4}$, converged results in the Wi range of interest are obtained. At this level of refinement, highly spatially resolved polymer stresses are obtained. Hence, the computed stresses utilizing this Lagrangian/BD procedure should provide a stringent test of the self-consistent computed stresses.

https://doi.org/10.1017/jfm.2011.504 Published online by Cambridge University Press

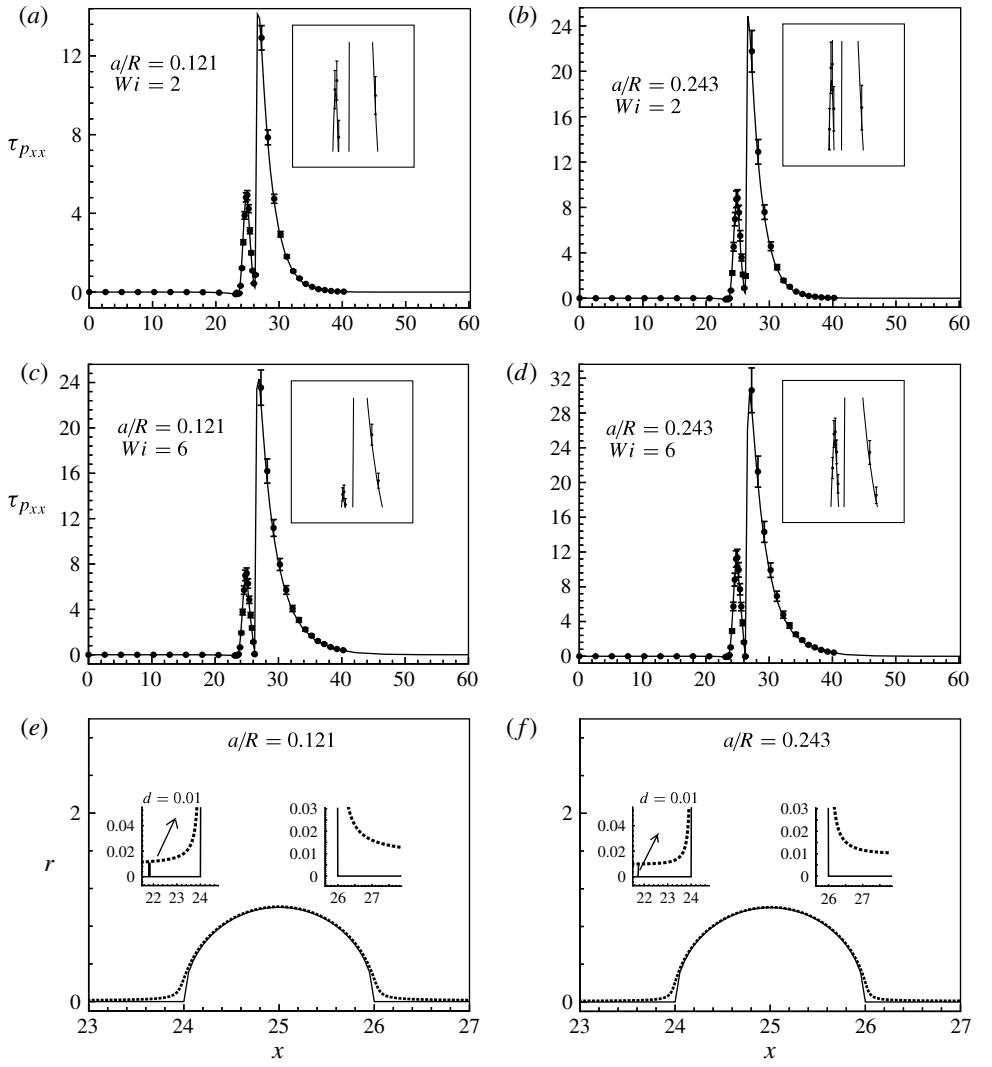


FIGURE 4. (*a–d*) Comparison of prototypical steady-state $\tau_{p_{xx}}$ profiles, for various a/R and Wi values, for the FENE model predicted using self-consistent simulations, solid line, and Lagrangian-based integration, circles, along streamlines shown in (*e*) and (*f*). Insets show magnification of $\tau_{p_{xx}}$ and streamlines.

Figure 4 depicts comparisons of prototypical steady-state $\tau_{p_{xx}}$ profiles along streamlines near the centreline of the tube in the vicinity of the sphere calculated using the mesh with 18 898 elements, with $b = 4000$. Overall, the excellent agreement between the self-consistent simulations and the Lagrangian-based results clearly demonstrates the accuracy of the self-consistent multiscale simulation results.

4.2. *Comparison of computed and experimentally measured drag correction factor*

Consistent with prior experimental findings, in this study the drag correction factor K is defined such that the steady-state drag force on the sphere is given by

$$F_D = 6\pi\eta_0 a U_s K \tag{4.1}$$

https://doi.org/10.1017/jfm.2011.504 Published online by Cambridge University Press

where the drag correction factor $K \equiv K(Wi, \chi)$. In the limit of $Wi \to 0$, K can be described by the well-known Faxen correction $K_N(\chi)$ for creeping motion of a sphere through a Newtonian liquid (Happel & Brenner 1973):

$$K_N(\chi) \equiv \frac{1}{1 - f(\chi)} \tag{4.2}$$

with

$$f(\chi) = [2.10444(\chi) - 2.08877\,(\chi)^3 + 0.94813\,(\chi)^5 + 1.372\,(\chi)^6 - \cdots]. \tag{4.3}$$

For $\chi = 0.243$ one obtains $K_N = 1.932$ and for $\chi = 0.121$, $K_N = 1.335$ (Happel & Brenner 1973; Arigo *et al.* 1995). These results are in good agreement with our simulated drag correction factors. Hence, they have been used to compute the normalized drag correction factor K/K_N where K is the computed drag correction factor. Care must be taken in comparing the results of numerical calculations with the experimentally measured values (Arigo *et al.* 1995). In purely experimental or purely numerical studies, the drag data are usually reduced to a plot of the drag correction factor $K(Wi, \chi)$ versus Wi. However as noted by Arigo *et al.* (1995) such a presentation is not very helpful when one is interested in comparing the experimental steady settling velocity of a sphere of given density though a viscoelastic fluid of known properties with steady-state numerical simulation since the unknown velocity appears in both the abscissa and the ordinate. In the experiments, spheres of varying densities are dropped in the fluid and the terminal velocity of the sphere is established when the reduced weight of the sphere (F_w) is exactly balanced by the drag force (F_D) exerted by the fluid. By contrast, in the simulations, the steady terminal velocity of the sphere and the relaxation time of the fluid (and hence the Wi) are specified *a priori*, and the force exerted by the fluid on the sphere in steady motion is calculated. Since this force must be balanced by the weight of the sphere, numerical calculations implicitly determine the density of the settling sphere required to attain a given Wi. The nonlinear variation in the drag correction factor with respect to the aspect ratio and Weissenberg number precludes simple interconversion between the two approaches. To resolve this issue, following earlier studies (Arigo *et al.* 1995), we have defined the dimensionless effective weight of the sphere in the experiments as $2a(\rho_s - \rho_f)g\lambda/9\eta_0$ which is equivalent to $Wi \times K(Wi, \chi)$ in the simulations. In turn, the flow properties computed via numerical simulations are compared with the experimental measurements at the Wi^* which gives the same value of the product $Wi^* \times K(Wi^*, \chi)$ as the experiment, i.e. $Wi_{exp} \times K_{exp}(Wi, \chi)$. In our calculations, the calculated and measured dimensionless weight match at multiple Wi where the difference between Wi^* and Wi_{exp} is less than 1 %. Therefore we are confident that a direct comparison of drag correction factor between our numerical predictions and experimental results can be performed.

As mentioned earlier, prior studies (Lunsmann *et al.* 1993; Satrape & Crochet 1994; Arigo *et al.* 1995; Rasmussen & Hassager 1996; Yang & Khomami 1999; McKinley 2001) have shown that simulations of a sphere sedimenting in a viscoelastic fluid with closed-form constitutive equations, for example the FENE-P model, are limited to $Wi < 3.0$ for highly strain-hardening fluids and even in the range where converged numerical solutions can be obtained the predicted drag coefficient as a function of Wi and χ is at best qualitative (Yang & Khomami 1999; McKinley 2001; Somasi 2001). In a recent study (Abedijaberi & Khomami 2011) the deficiencies of closed-form constitutive equations in providing realistic macroscopic flow property predictions in flows past bluff objects has been thoroughly investigated and it has been shown that

https://doi.org/10.1017/jfm.2011.504 Published online by Cambridge University Press

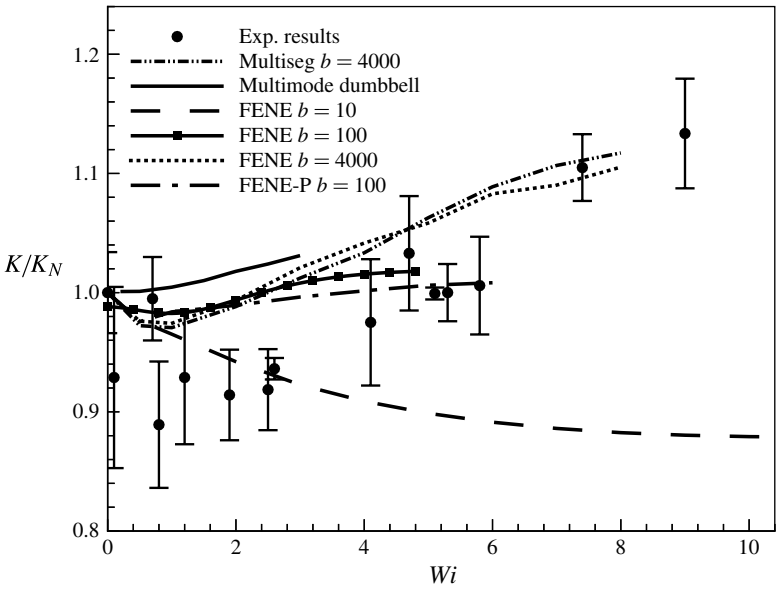


FIGURE 5. Comparison of the experimentally obtained steady-state normalized drag coefficient correction factor with the corresponding values obtained from FENE and FENE-P calculations at $\chi = 0.121$.

extremely large stress gradients along the plane of symmetry in the wake of the sphere observed in FENE-P-based computations leads to breakdown of numerical simulations at $Wi \approx 1$ for significantly strain-hardening fluids, i.e. $b > 300$. Consequently, in earlier studies aimed at simulating the aforementioned experiments, unrealistically low values of b (not consistent with the molecular parameters of PB used in the test fluid) were used in order to obtain converged results in the region where significant drag enhancement in the experiments was observed. Hence, the simulations were unable to capture the drag enhancement quantitatively. In this study for the first time we have computed the drag on the sphere at high Wi with b values that are consistent with the molecular description of the PB used in the test fluid (McKinley *et al.* 1993). To do so we have used the FENE model in meshes with appropriately small elements near both stagnation points of the sphere. Specifically, beside the commonly observed steep stress boundary layer for highly strain-hardening fluids near the rear stagnation point which forms at $Wi \approx 1$, one also observes a stress boundary layer close to the front stagnation point at $Wi \approx 3$ for $b = 4000$ which needs to be numerically resolved, otherwise it would lead to breakdown of simulations irrespective of how refined the mesh is near the rear stagnation point.

The normalized drag correction factor predicted by the FENE dumbbell model as well as the experimentally measured values (Arigo *et al.* 1995) as a function of Wi are shown in figures 5 and 6 for $\chi = 0.121$ and $\chi = 0.243$ respectively. The drag correction factor for $b = 10$ decreases monotonically while for $b = 100$ and $b = 4000$, the FENE dumbbell model predicts a slight decrease followed by monotonic increase in drag correction factor. This difference in the trend in the computed drag correction factor versus Wi for small and large b values is consistent with earlier studies (Yang & Khomami 1999; McKinley 2001). However, as can be seen in figures 5 and 6, the FENE dumbbell model with $b = 4000$ provides a good prediction of the drag on the sphere.

https://doi.org/10.1017/jfm.2011.504 Published online by Cambridge University Press

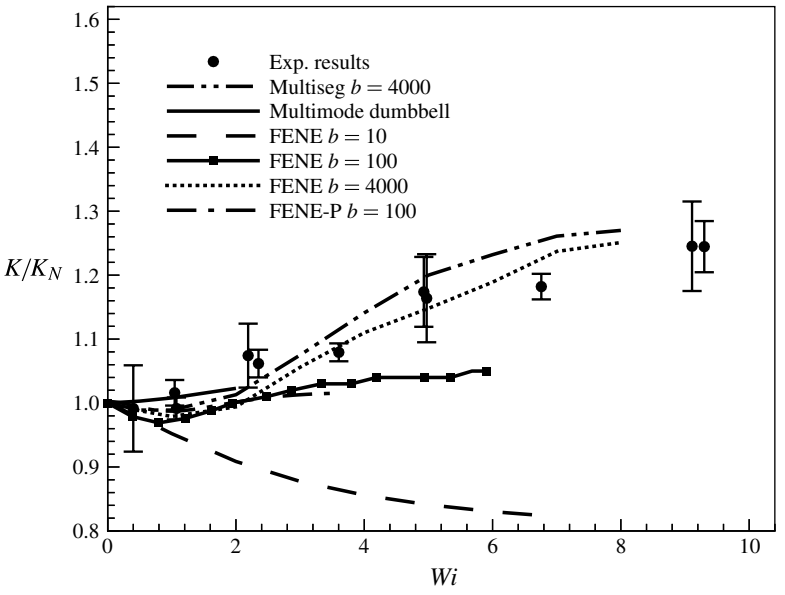


FIGURE 6. Comparison of the experimentally obtained steady-state normalized drag coefficient correction factor with the corresponding values obtained from FENE and FENE-P calculations at $\chi = 0.243$.

Although the FENE dumbbell model with small b captures the decrease in the measured drag coefficient at $Wi \approx 1$ it fails to predict the significant increase in the drag at high Wi, while simulations with large b do a very good job of describing the experimental data over the entire range of Wi. However, they give rise to an overprediction of the measured drag coefficient at $1 < Wi < 4$. To this end we have performed simulations with a three-mode model (see table 2 for more details). The results of these three-mode FENE dumbbell simulations are also shown in figures 5 and 6. Clearly, the drag correction factor predicted by the three-mode FENE dumbbell model, using the parameters given in table 2, increases monotonically as a function of Wi, for both χ values. In fact, the predicted drag is significantly higher than both the experimentally measured values and computations based on a single-mode dumbbell model. To elucidate the physical underpinning of this observation, we have plotted the probability density function (p.d.f.) of polymer molecule end-to-end distance predicted by single- and three-mode FENE models using different b values at the point of maximum stress downstream of the rear stagnation point. As can be seen in figures 7 and 8 smaller polymer molecules are stretched at lower Wi. Specifically, in a single-mode calculation with $b = 10$, the molecules are stretched at $Wi \approx 0.5$ while at $b = 100$ and $b = 4000$ the molecules are near their equilibrium configuration for $Wi \leqslant 1$. On the other hand, due to the way that $Wi_{mean} = U\lambda_{mean}/a$ is defined in the three-mode calculations (see table 2), the polymer molecules of the modes with $\lambda_i/\lambda_{mean} > 1$ experience Wi_{eff} which is larger than Wi_{mean} and consequently get fully stretched at lower Wi_{mean} compared to a single-mode description.

Consequently, even at small Wi the mode with the longest relaxation time dominates the contribution of various modes to the polymeric stresses; hence, the system effectively behaves as a single dumbbell with $b = 4000$ with a higher relaxation time, i.e. $\lambda = 2.84$. In fact the drag correction factor predicted with a dumbbell model

https://doi.org/10.1017/jfm.2011.504 Published online by Cambridge University Press

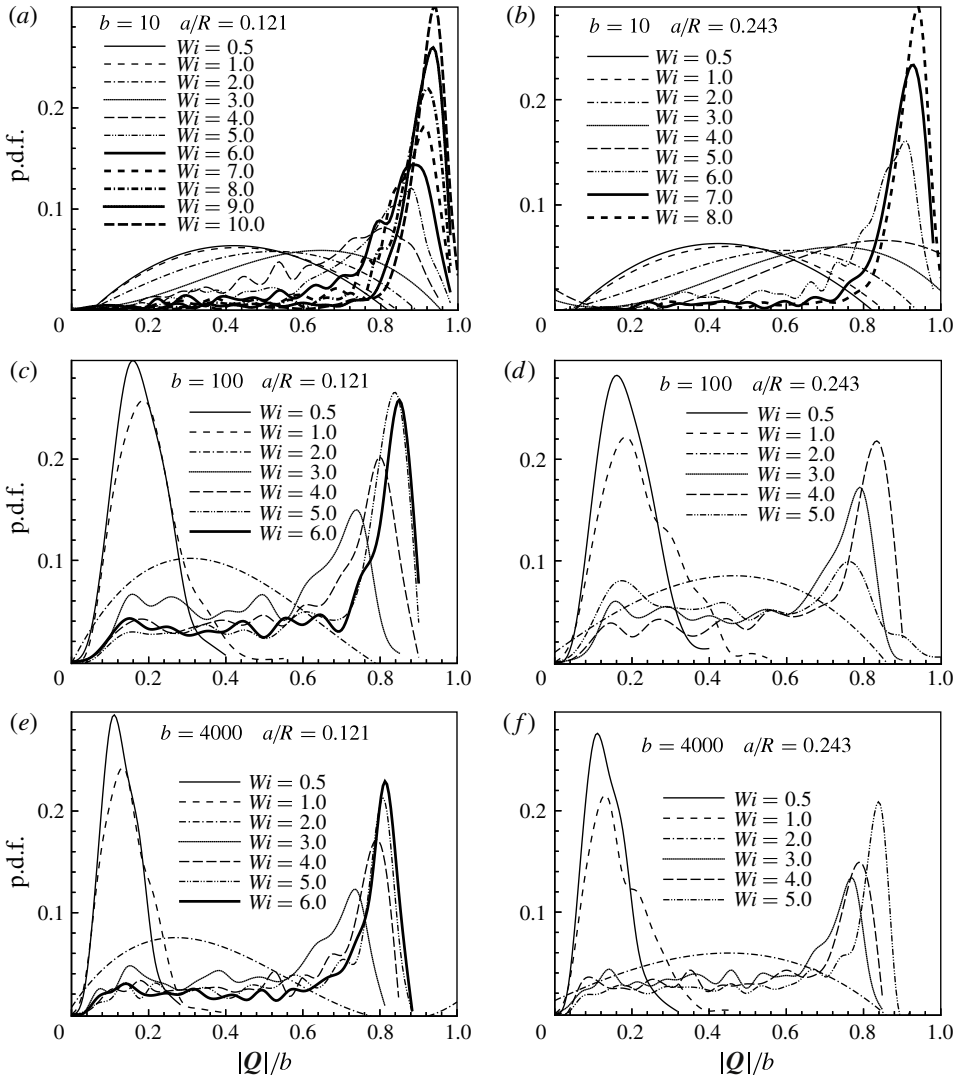


FIGURE 7. Probability density function (p.d.f.) of non-dimensionalized end-to-end distance $|\boldsymbol{Q}|/b$ at the point of maximum stress downstream of the rear stagnation point of the sphere predicted by the single-mode FENE dumbbell model for various b and a/R values.

with $b = 4000$ is reproduced closely by shifting the three-mode calculation results by a factor of 2.84/0.7925. To this end, the p.d.f. of polymer molecules of each mode in a three-mode calculation is compared with a single-mode calculation with the same b (see figure 9). The comparison is performed at Wi_{mean} where the Wi_{eff} polymer molecules are experiencing is close to the Wi of single-mode calculations. The similarity between the p.d.f.s clearly suggests that different modes function nearly independently of each other in the three-mode simulations. This suggests that in strong straining flows the coupling of polymer dynamics with momentum equations does not give rise to significant mode–mode interaction through modifications of the flow kinematics. This observation has motivated examination of micromechanical models that allow implicit mode–mode coupling. The simplest model with this feature is the

https://doi.org/10.1017/jfm.2011.504 Published online by Cambridge University Press

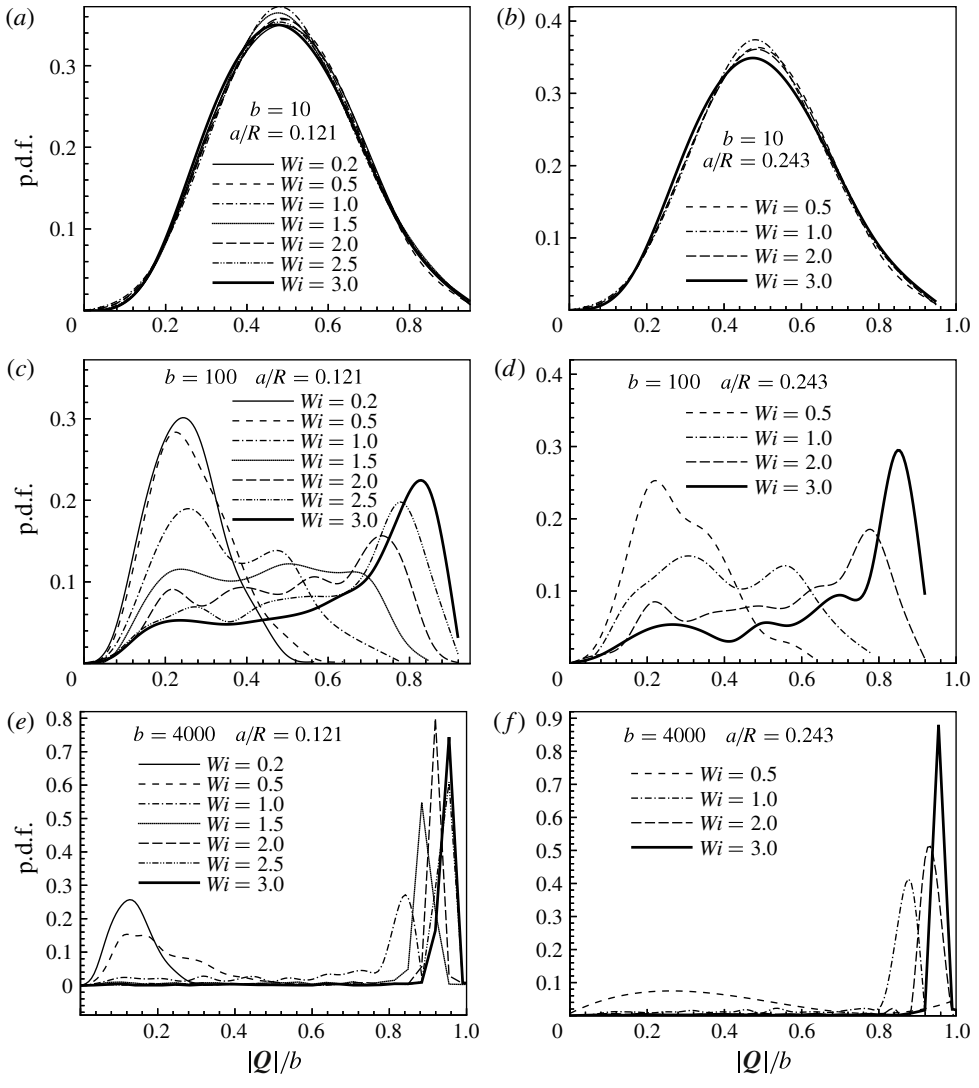


FIGURE 8. Probability density function (p.d.f.) of non-dimensionalized end-to-end distance $|\boldsymbol{Q}|/b$ at the point of maximum stress downstream of the rear stagnation point of the sphere predicted by the three-mode FENE dumbbell model for various b and a/R values.

bead–spring chain model composed of N beads and $N-1$ springs. Specifically, the use of this model allows both configurational diversity and mode–mode coupling, which have been shown to be essential in quantitatively describing macromolecular dynamics in simple kinematics flows (Doyle *et al.* 1998; Shaqfeh 2005; Larson 2005).

The normalized drag correction factor predicted by the three-segment FENE bead–spring chain model as a function of Wi and χ is also shown in figures 5 and 6. Overall, the predicted drag at high Wi is slightly higher than the single-segment model and somewhat smaller at lower Wi (more aligned with the experimental measurements). To more closely examine the differences between the predictions of the single-segment dumbbell and the multi-segment chain models, the p.d.f. of the end-to-end distance for both models is shown in figure 9. Clearly, the polymer molecules near the rear

https://doi.org/10.1017/jfm.2011.504 Published online by Cambridge University Press

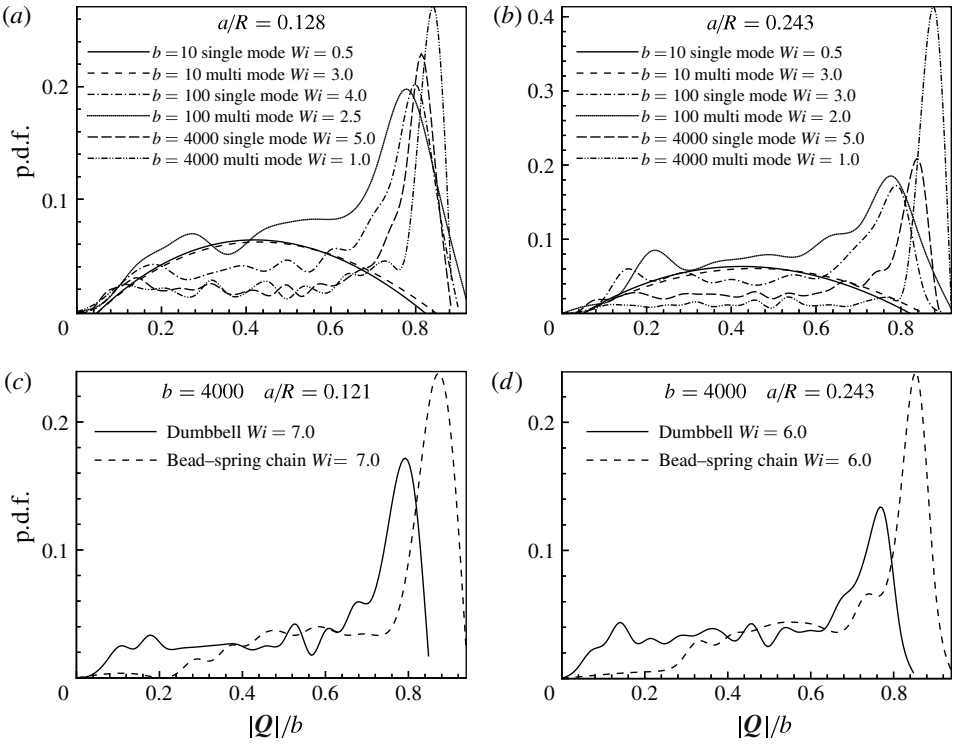


FIGURE 9. Probability density function (p.d.f.) of non-dimensionalized end-to-end distance $|\boldsymbol{Q}|/b$ at the point of maximum stress downstream of the rear stagnation point of the sphere for various b and a/R values.

stagnation point of the sphere described by the FENE bead–spring chain model are more stretched compared to the FENE dumbbell model, which clearly suggests the existence of distinct flow microstructure coupling at different levels of coarse graining (see figure 9). This intricate coupling also influences the total traction ($\boldsymbol{n} \cdot \boldsymbol{\tau} \cdot \boldsymbol{e}_x$) on the sphere and its components, i.e. polymeric and viscous deviatoric stresses as well as the pressure. In fact, the total traction along the surface of the sphere shows significant localization near the rear stagnation point (see figures 10 and 11). Consequently, the effect of distinct flow microstructure couplings predicted by various FENE dumbbell and chain models on the drag is mainly limited to the region near the rear stagnation point of the sphere. Since the drag is obtained by integration of the traction over the entire surface of the sphere, this measure cannot accurately capture the overall effect of fluid elasticity on the flow dynamics predicted by the FENE dumbbell and three-segment chain models. However, as will be shown later, the aforementioned flow microstructure coupling has a very significant effect on the wake structure.

In order to better understand the mechanism of the drag enhancement we have examined the contribution of polymeric and viscous deviatoric stresses as well as the pressure to the drag coefficient, i.e. K^E, K^V and K^P respectively (Yang & Khomami 1999). Overall, polymeric stresses tend to give rise to a reduction in the drag coefficient while viscous stresses give rise to an increase in the drag coefficient. However, the trend in the variation of drag coefficient as a function of Wi more or less follows the variations observed in the pressure contribution to the drag, particularly at

https://doi.org/10.1017/jfm.2011.504 Published online by Cambridge University Press

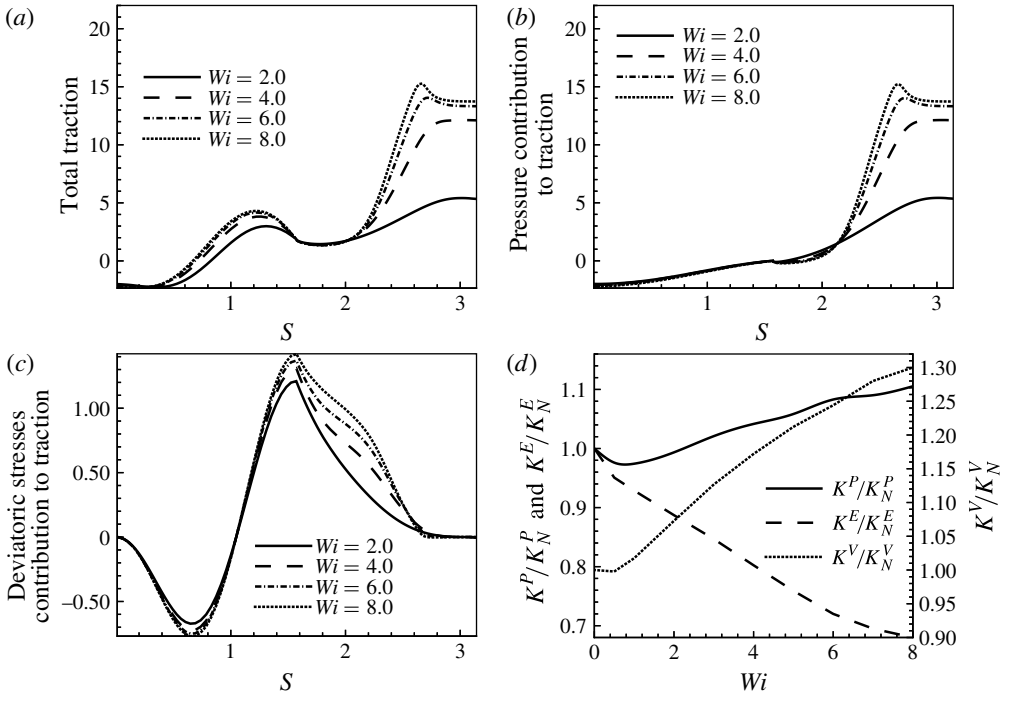


FIGURE 10. (*a–c*) The contribution of polymeric and viscous deviatoric stresses as well as the pressure to the traction on the surface of the sphere as a function of the position along the surface of the sphere (*d*) and total drag on the sphere as a function of *Wi* predicted by the three-segment FENE bead–spring chain model at $\chi = 0.121$.

high *Wi*. This indicates that the pressure, particularly near the rear stagnation point, is the dominant factor in determining the overall drag on the sphere at high *Wi* (see figures 10*d* and 11*d*).

4.3. *Elastic effects on the structure of the wake*

In addition to an integrated property such as the drag on the sphere, which has been shown not to be a very sensitive measure of elastic effects on the overall flow (McKinley 2001), a number of studies have investigated the influence of flow elasticity on the velocity and stresses in the wake of bluff objects. Specifically, experiments show that the axial extent of this elastic wake depends on both *Wi* and χ and decays slowly over a distance of 30 radii for the highest reported *Wi*, i.e. $Wi = 9.092$ for $\chi = 0.243$ and $Wi = 7.557$ for $\chi = 0.121$ (Arigo *et al.* 1995; McKinley 2001). It has also been shown that continuum calculations with dumbbell-based models can at best qualitatively capture the wake structure. Specifically, the extent of wake structure is highly underpredicted (limited to 2–3 radii downstream of the sphere) (Arigo *et al.* 1995; McKinley 2001).

In figure 12 the axial centreline velocity upstream and downstream of the spheres calculated by FENE dumbbell and chain models is depicted for both χ values. As expected at low *Wi* the velocity field exhibits fore/aft symmetry. However, as *Wi* is enhanced, the velocity field progressively loses its fore/aft symmetry and a viscoelastic wake develops. Overall, the FENE chain model predicts a much more elongated wake structure than the dumbbell model. Specifically the distances predicted by FENE

https://doi.org/10.1017/jfm.2011.504 Published online by Cambridge University Press

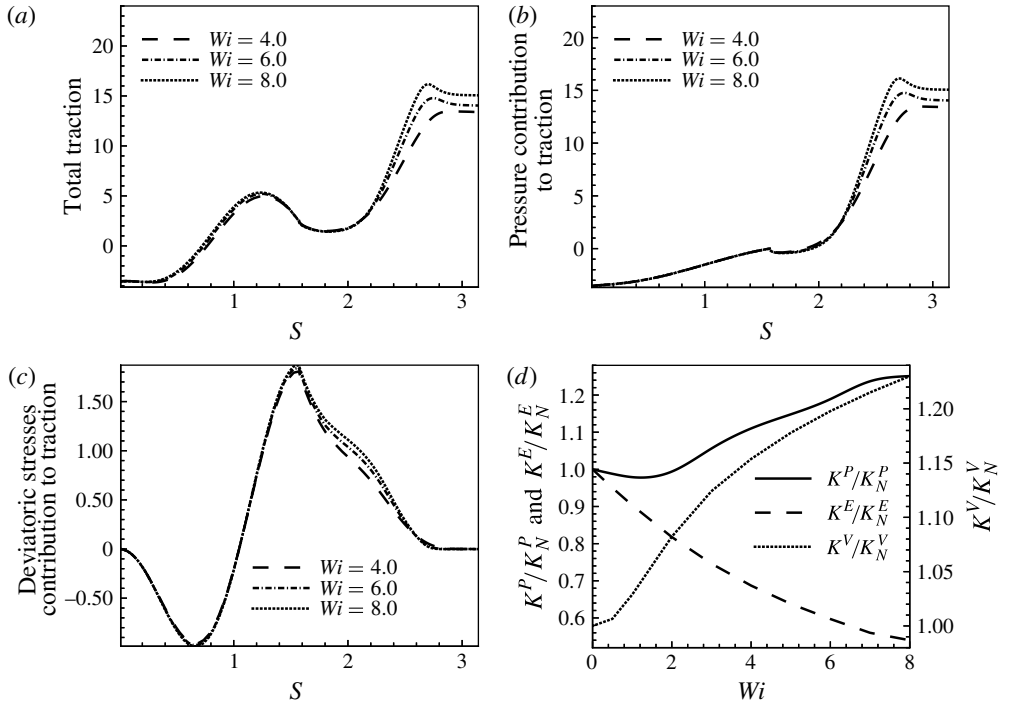


FIGURE 11. (*a–c*) The contribution of polymeric and viscous deviatoric stresses as well as the pressure to the traction on the surface of the sphere as a function of the position along the surface of the sphere (*d*) and total drag on the sphere as a function of Wi predicted by the three-segment FENE bead–spring chain model at $\chi = 0.243$.

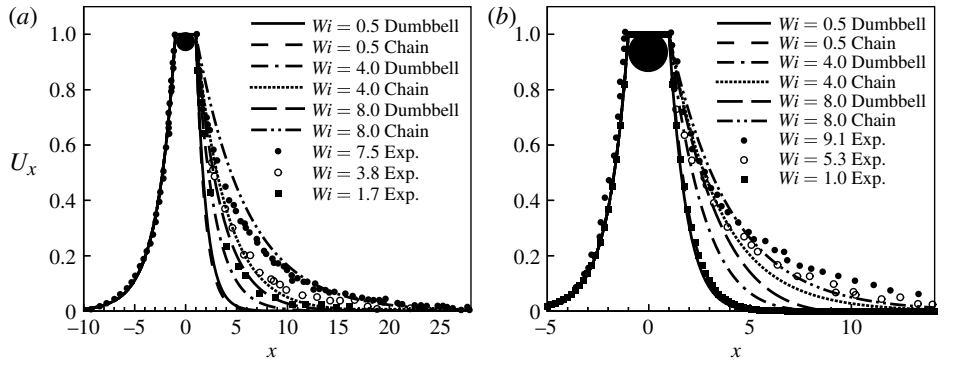


FIGURE 12. Predicted velocity along the centreline of the tube and the surface of the sphere at (*a*) $\chi = 0.121$ and (*b*) $\chi = 0.243$; $b = 4000$.

dumbbell and chain models for the velocity to decay to its equilibrium value are approximately 15 and 25 for $\chi = 0.121$ and 8 and 15 for $\chi = 0.243$ at $Wi = 8.0$, respectively. The superior predictions of the chain models can be rationalized by its more accurate description of the macromolecular dynamics in the fast transient extensional flows in the wake of the sphere. This, in turn, leads to a more accurate description of the polymer body force that gives rise to the extended velocity wake.

https://doi.org/10.1017/jfm.2011.504 Published online by Cambridge University Press

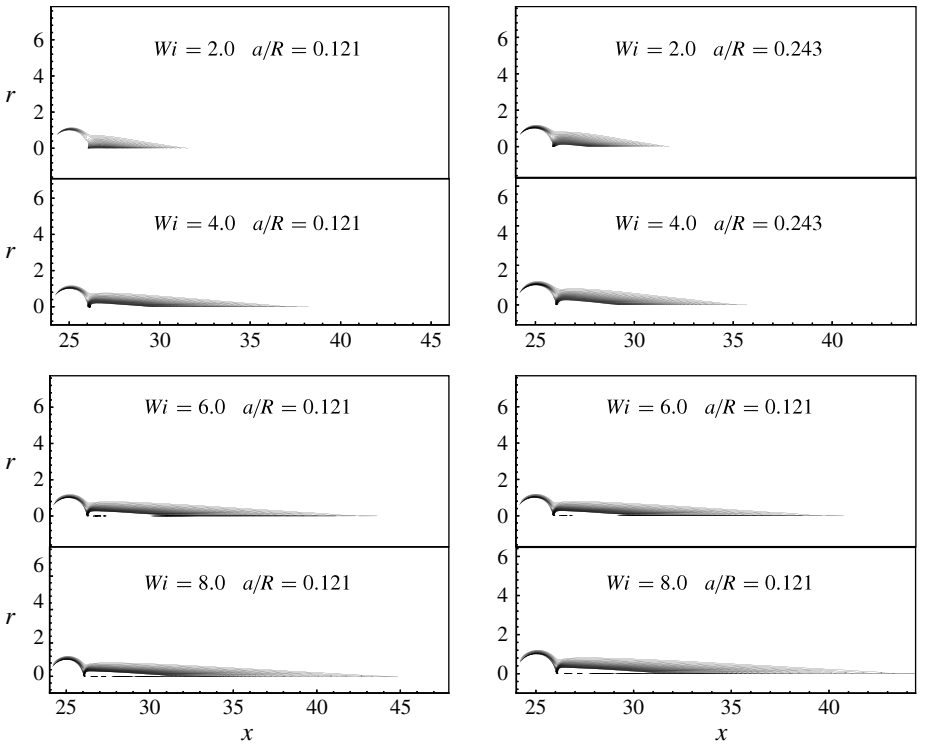


FIGURE 13. Stress ($\tau_{p_{xx}}$) contour plots in the wake of the sedimenting sphere (multi-segment bead–spring FENE model with $b = 4000$). To facilitate the comparison all the results are plotted in the same range and number of levels, i.e. 50 levels in the 1–10 range.

However, this extended velocity wake is still 5–10 % shorter than actual measurements and we believe that a more quantitative prediction of the experimental data requires simulations with bead–spring chains with more than three segments.

Birefringence measurements can also be used to study the influence of fluid elasticity on the wake structure behind bluff objects. In fact, the presence of a high level of molecular orientations, dubbed 'birefringent strands', in the wake of a cylinder confined in a channel up to 10 radii downstream of the cylinder has been observed for polymeric solutions at $Wi \approx 2$ (Baaijens *et al.* 1995). To examine the extent of the birefringent strand in the sedimenting sphere problem, we have examined the stress contours in the wake of the sphere (see figure 13). Clearly, the bead–spring chain model predicts strands which extend dramatically with increasing Wi at both χ values and even reach the end of computational domain, i.e. 60 radii, for $Wi \approx 8$.

5. Summary

Self-consistent multiscale flow simulations of a highly elastic dilute polymeric solution, described by first-principles micromechanical models for sedimentation of a sphere in a tube filled with a dilute polymeric solution have been performed. Through comparisons with experimental measurements, we have demonstrated that the evolution of the drag coefficient as a function of fluid elasticity can be accurately predicted when the macromolecular dynamics is described by realistic micromechanical models that closely capture the transient extensional viscosity of

https://doi.org/10.1017/jfm.2011.504 Published online by Cambridge University Press

the experimental fluid at high extension rates. Specifically, for the first time we have computed the drag coefficient on the sphere at high *Wi* utilizing multi-segment bead-spring chain models with appropriate molecular parameters and have demonstrated that hi-fidelity multiscale simulation is not only capable of accurately describing the drag on the sphere as a function of *Wi* at various sphere-to-tube diameter ratios but also it can closely reproduce the experimentally observed velocity and stresses in the wake of the sphere.

Acknowledgements

B.K. would like to thank NSF for supporting this work through grant CBET-0755269. This research was also supported by an allocation of advanced computing resources provided by the National Science Foundation. The computations were performed on Kraken at the National Institute for Computational Sciences.

REFERENCES

ABEDIJABERI, A. & KHOMAMI, B. 2011 On the limitations of elastic dumbbell based constitutive equations in simulation of flow of dilute polymeric solutions with stagnation points. *J. Non-Newtonian Fluid Mech.* **166**, 533–545.

ABEDIJABERI, A., SOULAGES, J., KROGER, M. & KHOMAMI, B. 2008 Flow of branched polymer melts in a lubricated cross-slot channel: a combined computational and experimental study. *Rheol. Acta* **48**, 97–108.

ARIGO, M. T., RAJAGOPALAN, D. R., SHAPELY, N. T. & MCKINLEY, G. H. 1995 The sedimentation of a sphere through an elastic fluid. Part I. Steady motion. *J. Non-Newtonian Fluid Mech.* **60**, 225–257.

BAAIJENS, F. P. T., BAAIJENS, H. P. W., PETERS, G. W. M. & MEIJER, H. E. H. 1994 An exprimental and numerical investigation of a viscoelastic flow around a cylinder. *J. Rheol.* **38**, 351–376.

BAAIJENS, H. P. W., PETERS, G. W. M., BAAIJENS, F. P. T. & MEIJER, H. E. H. 1995 Viscoelastic flow past a confined cylinder of a polyisobutylene solution. *J. Rheol.* **39**, 1243–1277.

BIRD, R. B., CURTISS, C. F., ARMSTRONG, R. C. & HASSAGER, O. 1987 *Dynamics of Polymeric Liquids,* Vol. 2. Wiley.

BROOKS, A. N. & HUGHES, T. J. R. 1982 Streamline Upwind/Petrov–Galerkin formulations for convection dominated flows with particular emphasis on the incompressible Navier–Stokes equations. *Comput. Meth. Appl. Mech. Engng* **32**, 199–259.

BURGHARDT, W. R., LI, J., YANG, B. & KHOMAMI, B. 1999 Uniaxial extensional characterization of a shear thinning fluid using axisymmetric flow birefringence. *J. Rheol.* **43**, 147–165.

DOYLE, P. S., SHAQFEH, E. S. G. & SPIEGELBERG, G. H. 1998 Relaxation of dilute polymeric solutions following extensional flow. *J. Non-Newtonian Fluid Mech.* **76**, 79–110.

GIGRAS, P. G. & KHOMAMI, B. 2002 Adaptive configuration fields: a new multiscale simulation technique for reptation-based models with a stochastic strain measure and local variations of life span distribution. *J. Non-Newtonian Fluid Mech.* **108**, 99–122.

GRILLET, A. M., YANG, B. & KHOMAMI, B. 1999 Modelling of viscoelastic lid driven cavity flow using finite element simulations. *J. Non-Newtonian Fluid Mech.* **88**, 99–131.

GUENETTE, R. & FORTIN, M. 1995 A new mixed finite element method for computing viscoelastic flows. *J. Non-Newtonian Fluid Mech.* **60**, 27–52.

HALIN, P., LIELENS, G., KEUNINGS, R. & LEGAT, V. 1998 The Lagrangian particle method for macroscopic and micro–macro viscoelastic flow computations. *J. Non-Newtonian Fluid Mech.* **77**, 153–190.

HAPPEL, J. & BRENNER, H. 1973 *Low Reynolds Number Hydrodynamics*. Martinus Nijhoff.

HARLEN, O. G., RALLISON, J. M. & CHILCOTT, M. D. 1990 High-Deborah-number flow of a dilute polymer solution past a sphere falling along the axis of a cylindrical tube. *J. Non-Newtonian Fluid Mech.* **33**, 157–173.

https://doi.org/10.1017/jfm.2011.504 Published online by Cambridge University Press

HULSEN, M. A., VAN HEEL, A. P. G. & VAN DEN BRULE, B. H. A. A. 1997 Simulation of viscoelastic flows usign Brownian configuration fields. *J. Non-Newtonian Fluid Mech.* **70**, 79–101.

KHOMAMI, B., TALWAR, K. K. & GANPULE, H. K. 1994 A comparative study of higher and lower order finite element techniques for computation of viscoelastic flows. *J. Rheol.* **38**, 255–289.

KOPPOL, A. P., SURESHKUMAR, R., ABEDIJABERI, A. & KHOMAMI, B. 2009 Anomalous pressure drop behaviour of mixed kinematics flows of viscoelastic polymer solutions: a multiscale simulation approach. *J. Fluid Mech.* **631**, 231–253.

KOPPOL, A. P., SURESHKUMAR, R. & KHOMAMI, B. 2007 An efficient algorithm for multiscale flow simulation of dilute polymeric solutions using bead-spring chains. *J. Non-Newtonian Fluid Mech.* **141**, 180–192.

LARSON, R. 2005 The rheology of dilute solutions of flexible polymers: progress and problems. *J. Rheol.* **49**, 1–70.

LASO, M. & ÖTTINGER, H. C. 1993 Calculation of viscoelastic flow using molecular models: the CONNFFESSIT approach. *J. Non-Newtonian Fluid Mech.* **47**, 1–20.

LI, J., BURGHARDT, W. R., YANG, B. & KHOMAMI, B. 1998 Flow birefringence and computational studies of a shear thinning polymer solution in axisymmetric stagnation flow. *J. Non-Newtonian Fluid Mech.* **74**, 151–193.

LI, J., BURGHARDT, W. R., YANG, B. & KHOMAMI, B. 2000 Birefringence and computational studies of a polystyrene Boger fluid in axisymmetric stagnation flow. *J. Non-Newtonian Fluid Mech.* **91**, 189–220.

LUNSMANN, W. J., GENISER, L., BROWN, R. A. & ARMSTRONG, R. C. 1993 Finite element analysis of steady viscoelastic flow around a sphere: calculations with constant viscosity models. *J. Non-Newtonian Fluid Mech.* **48**, 63–99.

MCKINLEY, G. H. 2001 *Transport Processes in Bubbles, Drops and Particles*. Taylor & Francis.

MCKINLEY, G. H., ARMSTRONG, R. C. & BROWN, R. A. 1993 The wake instability in viscoelastic flow past confined circular cylinders. *Phil. Trans. R. Soc. Lond.* A **344**, 265–304.

ÖTTINGER, H. C., VAN DEN BRULE, B. H. A. A. & HULSEN, M. A. 1997 Brownian configuration fields and variance reduce CONNFFESSIT. *J. Non-Newtonian Fluid Mech.* **70**, 255–261.

PERKINS, T. T., SMITH, D. E. & CHU, S. 1997 Single polymer dynamics in an elongational flow. *Science* **276**, 2016–2021.

QUINZANI, L. M., ARMSTRONG, R. C. & BROWN, R. A. 1994 Birefringence and laser-doppler velocimetry (LDV) studies of viscoelastic flow through a planar contraction. *J. Non-Newtonian Fluid Mech.* **52**, 1–36.

RASMUSSEN, H. K. & HASSAGER, O. 1996 On the sedimentation velocity of spheres in a polymeric liquid. *Chem. Engng Sci.* **51**, 1431–1440.

ROTHSTEIN, J. P. & MCKINLEY, G. H. 1999 Extensional flow of a polystyrene Boger fluid through a 4:1:4 contraction/expansion. *J. Non-Newtonian Fluid Mech.* **86**, 61–88.

ROTHSTEIN, J. P. & MCKINLEY, G. H. 2001 The axisymmetric contraction–expansion: the role of extensional rheology on vortex growth dynamics and the enhanced pressure drop. *J. Non-Newtonian Fluid Mech.* **98**, 33–63.

SATRAPE, J. V. & CROCHET, M. J. 1994 Numerical simulation of the motion of a sphere in a Boger fluid. *J. Non-Newtonian Fluid Mech.* **55**, 91–111.

SHAQFEH, E. S. G. 2005 The dynamics of single-molecule DNA in flow. *J. Non-Newtonian Fluid Mech.* **130**, 1–28.

SOMASI, M. 2001 Dynamics of polymeric fluids, a combined Brownian dynamics finite element approach. PhD Thesis, Washington University in St Louis.

SOMASI, M. & KHOMAMI, B. 2000 Linear stability and dynamics of viscoelastic flows using time-dependent stochastic simulation techniques. *J. Non-Newtonian Fluid Mech.* **93**, 339–362.

SOMASI, M. & KHOMAMI, B. 2001 A new approach for studying the hydrodynamic stability of fluids with microstructure. *Phys. Fluids* **13**, 1811–1814.

SOMASI, M., KHOMAMI, B., WOO, N. J., HUR, J. S. & SHAQFEH, J. S. 2002 Brownian dynamics simulations of bead-rod and bead-spring chains: numerical algorithms and coarse-graining issues. *J. Non-Newtonian Fluid Mech.* **108**, 227–255.

SZABÓ, B. & BABUŠKA, IVO 1987 *Finite Element Analysis*. John Wiley and Sons Inc.

https://doi.org/10.1017/jfm.2011.504 Published online by Cambridge University Press

SZADY, M. J., SALAMON, T., LIU, A. W., BORNSIDE, D. E, ARMSTRONG, R. C. & BROWN, R. A. 1995 A new mixed finite element method for viscoelastic flows governed by differential constitutive equations. *J. Non-Newtonian Fluid Mech.* **59**, 215–243.

TALWAR, K. K., GANPULE, H. K. & KHOMAMI, B. 1994 A note on the selection of spaces in computation of viscoelastic flows using the hp-finite element method. *J. Non-Newtonian Fluid Mech.* **52**, 293–307.

TALWAR, K. K. & KHOMAMI, B. 1992 Application of higher order finite element methods to viscoelastic flow in porous media. *J. Rheol.* **36**, 1377–1416.

TALWAR, K. K. & KHOMAMI, B. 1995 Flow of viscoelastic fluids past periodic square arrays of cylinders: inertial and shear thinning viscosity and elasticity effects. *J. Non-Newtonian Fluid Mech.* **57**, 197–202.

THOMAS, D. G., DEPUIT, R. J. & KHOMAMI, B. 2009 Simulations of single DNA molecules in oscillatory shear flow. *J. Rheol.* **53**, 275.

VENKATARAMANI, V., SURESHKUMAR, R. & KHOMAMI, B. 2008*a* Coarse-grained modelling of macromolecular solutions using a configuration-based approach. *J. Rheol.* **52**, 1143.

VENKATARAMANI, V., SURESHKUMAR, R. & KHOMAMI, B. 2008*b* A computationally efficient approach for Hi fidelity fine graining from bead-spring models to bead-rod models. *J. Non-Newtonian Fluid Mech.* **149**, 20–27.

VERHOEF, M. R. J., VAN DEN BRULE, B. H. A. A. & HULSEN, M. A. 1999 On the modelling of a PIB/PB Boger fluid in extensional flow. *J. Non-Newtonian Fluid Mech.* **80**, 155–182.

WAPPEROM, P., KEUNINGS, R. & LEGAT, V. 2000 The backward-tracking Lagrangian particle method for transient viscoelastic flows. *J. Non-Newtonian Fluid Mech.* **91**, 273–295.

WIEST, J. M. & TANNER, R. I. 1989 Rheology of bead-nonlinear spring chain macromolecules. *J. Rheol.* **33**, 281–316.

YANG, B. & KHOMAMI, B. 1999 Simulation of sedimentation of a sphere in a viscoelastic fluid using molecular based constitutive models. *J. Non-Newtonian Fluid Mech.* **82**, 429–452.

https://doi.org/10.1017/jfm.2011.504 Published online by Cambridge University Press